I&EC research
Industrial & Engineering Chemistry Research

pubs.acs.org/IECR

Article

Fabrication of Iron-Magnesite under Mild Conditions through Indirect Carbonation of Peridotite and Its Utilization as a Partial Substitute for Cement in Concrete

German Montes-Hernandez,* Jérôme Weiss, Sarah Clavier, Benoît Cordonnier, Paul Tafforeau, Olivier Plé, and François Renard

Cite This: https://doi.org/10.1021/acs.iecr.5c00744

Read Online

ACCESS | Metrics & More | Article Recommendations | Supporting Information

ABSTRACT: The precipitation of magnesite and dolomite from aqueous media is challenging kinetically because several hydrated or hydroxylated Mg-carbonate phases can retard or inhibit the formation of these "enigmatic" minerals under so-called mild conditions ($T \leq 90$ °C and atmospheric pressure). Here, we demonstrate that Fe-magnesite can be synthesized at 60 °C in only 2 days via indirect carbonation of peridotite, following an amorphous-to-nesquehonite-to-magnesite transformation route. In this reactive configuration, the magnesite production time is significantly reduced from 2 days to only 6 h when the temperature is increased to 90 °C. The discovery of these mild conditions for magnesite production is a promising result because currently these temperatures can be reached by free-carbon energies. We also assess the incorporation of a fabricated magnesite-rich material at 90 °C as a partial cement substitute in concrete manufacturing. Preliminary results show that substituting 15 wt % of cement with magnesite-rich material could significantly reduce the CO_2 footprint with minimal impact on the concrete's mechanical-textural properties, including Young's modulus, strength, and macroporosity. In practice, this circular carbon approach could provide a dual advantage—reduced clinker production and permanent CO_2 storage—and present a significant opportunity to lower the carbon footprint of cement production.

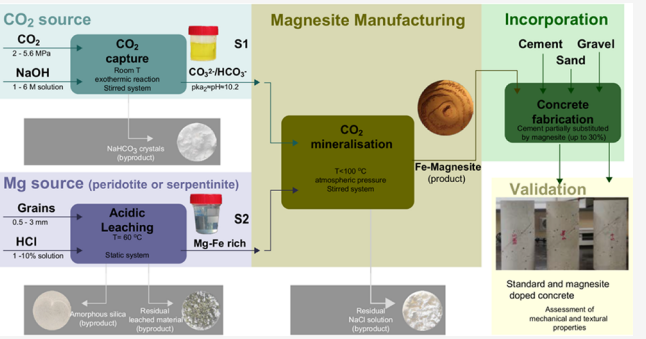

1. INTRODUCTION

Approximately 38 ± 3 Gt of CO_2 from fossil fuel consumption and industrial activities are emitted annually, representing an increase of about 67% since the 1990s. While natural cycles such as photosynthesis and chemisorption in soils and oceans help mitigate this production, a significant surplus remains, contributing to global warming, ocean acidification and major disruptions of ecosystems and climate.[1] Concrete is the most widely manufactured material, with production reaching 20 Gt/year. Portland cement accounts for 36% of the 7.7 Gt of CO_2 emissions released in 2010 by construction activities[2] and approximately 8% of total anthropogenic CO_2 emissions.[3] Decarbonizing the cement industry is crucial for reducing greenhouse gas emissions, as its CO_2 emissions primarily arise from energy consumption (~1/3) and the calcination of limestone (~2/3) during clinker fabrication.[2−6] While the first source can be significantly reduced with low-carbon energies, direct emissions of CO_2 from calcination present more profound challenges. In this context, CO_2 capture from industrial sources (e.g., cement production, metallurgy, and power plants) and its transformation into reusable products (e.g., ethanol, syngas, etc.) and/or nonenergetic materials (e.g., magnesite, dolomite, calcite, siderite, and other stable anhydrous carbonates) has been proposed as a means to stabilize CO_2 concentration in the atmosphere.[1,7−10] These measures help maintain a low carbon balance while supporting the transition to carbon-free energy sources.[11]

Ex-situ mineral trapping, the process of indirectly carbonating raw peridotite, serpentinites, basalts or mining wastes to produce readily usable stable and anhydrous Mg-carbonates (e.g., magnesite, iron-magnesite, dolomite, and ankerite), is a promising strategy for significantly reducing industrial CO_2 emissions and aligns with international carbon capture, utilization, and storage programs.[1,7−15] Notably, raw materials/rocks and/or mining wastes containing high concentrations of Mg and other divalent cations such as Fe and Ca, essential for producing stable carbonates, are abundant worldwide.[13] However, optimizing process conditions to produce magnesite-

Received: February 21, 2025
Revised: June 19, 2025
Accepted: June 23, 2025

rich carbonates under mild conditions and validating their specific applications remain significant challenges.

Magnesite ($MgCO_3$), dolomite ($MgCa(CO_3)_2$) and magnesite-rich solid solutions ($Mg_{1-x}M_xCO_3$, where M indicates Fe^{2+} and Ca^{2+}) are the most stable-anhydrous carbonate minerals under typical Earth surface conditions, with the highest resistance to leaching and weathering.[8] For example, the dissolution rates of magnesite and dolomite are 100−1000 times lower than that of calcite ($CaCO_3$) across a wide range of conditions, from ambient temperature to 150 °C and pH levels ranging from 1 to 14. Thus, these engineered anhydrous Mg carbonates are considered highly relevant minerals for the permanent storage of anthropogenic carbon dioxide. Moreover, both minerals are ready for use as profitable construction materials, filler mineral additives, and flame retardants.[8,16] The precipitation kinetics of magnesite and dolomite (ordered double carbonates) have been widely studied since their abiotic precipitation at ambient temperature (~25 °C) is virtually impossible within feasible experimental time scales.[8,16−18] This contrast strongly with anhydrous calcium carbonates (calcite, aragonite and vaterite) than can be easily formed at room temperature under abiotic conditions.[17] The strong solvation shell of magnesium ions in aqueous media plays an essential role in this limitation (ref 18 and references therein). However, the sole effect of magnesium hydration may not be the only factor inhibiting magnesite and dolomite formation. For dolomite, for example, recent studies claim that a strong-energetic crystallization barrier prevents the formation and/or regular Ca-Mg alternation in a long-range of crystal structure at ambient conditions. The fluid chemistry seems also to have an important influence on the magnesite and dolomite formation under mild conditions (e.g., [16−18]). In this context, studies have revealed that carbonate speciation close to pK_{a2} (pH ~ 10.3), high ionic concentration (<1M), and the presence of other competitive divalent cations and counterions accelerate the formation of magnesite and proto-dolomite under ambient and moderate temperatures (≤90 °C).[18,19] Other studies have reported magnesite precipitation under mild conditions, but in general, catalytic agents (biotic and abiotic) are used, and several days or weeks are required.[20−22]

To overcome these above limitations, we have developed a novel circular-material-flow laboratory method for the fabrication of liter-scale amounts of iron-magnesite under mild conditions ($T \leq 90$ °C and atmospheric pressure), within short time frames of 1 to 48 h, via indirect carbonation of peridotites. In this way, the technological readiness level (TRL) of our process is close to 2, but promising basic research was obtained because specific physicochemical mild conditions were discovered on the magnesite formation at 60 °C via direct transformation of nesquehonite into magnesite. In complement, hydrothermal conditions up to 200 °C under saturation pressure were also tested for kinetic comparison.

The primary target product is iron-magnesite, as this anhydrous mineral has multiple applications (e.g., 8). For instance, it can serve as partial substitute for cement during concrete fabrication, significantly reducing CO_2 emissions from the cement industry (e.g., 23−25) Additionally, other products of industrial interest can be obtained via this process. For example, nesquehonite ($MgCO_3 \cdot 3H_2O$), a promising green building material,[13,26] can be produced at room temperature when peridotite is leached. Alternatively, siderite ($FeCO_3$) and nesquehonite are preferentially formed when a basalt-rich material is used in the leaching step. In this way, we also assess the use of produced iron-magnesite at 90 °C as a partial substitute of cement in concrete fabrication. Herein, Young's modulus, strength and macro-porosity were determined on cylindrical concrete samples in order to assess the impact of magnesite substitution on the concrete performance. Magnesite produced at 90 °C was chosen because only 5−6 h are required for their synthesis. In the present study, iron-magnesite material refers to magnesite containing up to 10% Fe(II) and minor proportions of adhered iron oxides nanoparticles containing Fe(III).

2. MATERIALS AND METHODS

2.1. *CO_2 Capture Step.* Concentrated NaOH solutions (from 1 to 6 M) were used to capture CO_2 as ionic species (CO_3^{2-} and HCO_3^-) at moderate pressure ($P_{CO2} \leq 55$ bar) and ambient temperature (25 °C). A specified amount of NaOH and 1 L of water were placed into a reactor cell with a 2 L capacity. Then, a defined amount of CO_2 was injected into the reactor at pressures from 10 to 55 bar. The pressure drop related to the CO_2 chemisorption process and the exothermicity (temperature increase during CO_2 chemisorption) were directly monitored in this anisobaric system. Isobaric conditions (20 bar) and sequential CO_2 injections (20 + 10 + 10... up to a cumulative total of 100 bar for higher NaOH concentrations) were also tested. In all cases, the maximum reaction duration was 24 h.

The optimization, reaction mechanisms, and kinetics were determined using time-resolved Raman spectroscopy measurements, as demonstrated in previous studies conducted in our group.[8,17−19] Real-time monitoring enabled better control of the carbonate speciation in the resulting alkaline solutions (CO_3^{2-}-rich solution, CO_3^{2-}/HCO_3^- mixed solution, and HCO_3^--rich solution). Moreover, $NaHCO_3$ crystalline-powdered byproducts that have several well-known industrial applications can also be directly obtained during the carbonation process of NaOH solutions.

2.2. Leaching Step. Divalent cations (mainly Mg and Fe) in solution were obtained from natural peridotite and a basalt-peridotite mixture (collected in France, Central Massif) through a simple leaching process using acidic (HCl) solutions. The ground samples (millimetric grains ranging from 0.6 to 5 mm) were treated with concentrated acidic HCl solutions (up to 10% concentration) at room and moderate temperatures (up to 60 °C) for varying durations (up to 10 days) in reactors without agitation (static system) in order to obtain Mg−Fe-rich solutions. Several experiments were conducted to optimize the reaction time, HCl concentration, solution-to-solid weight ratio, and temperature. In the present study, raw rocks were used as the source of divalent cations; however, many industrial wastes, such as steel slags, mining waste (except carbonates or sedimentary rocks), and asbestos waste, could also be used and are generally more reactive than raw rocks.

2.3. *CO_2 Mineralization or Carbonate Precipitation Step.* Solutions obtained from CO_2 capture (preferentially alkaline CO_3^{2-}/HCO_3^- solution with concentrations close to pK_{a2}) and from the leaching step (Mg−Fe-rich acidic solution) were then used to precipitate stable carbonates (preferably anhydrous) by controlled mixing (at a given addition rate, 2−12 mL/min) of the two solutions. The main objective was to produce magnesite and Mg−Fe anhydrous carbonates at moderate temperatures (<90 °C) preferably, or at higher temperatures (up to 200 °C) within a reduced time. Several of

https://doi.org/10.1021/acs.iecr.5c00744
Ind. Eng. Chem. Res. XXXX, XXX, XXX−XXX

Table 1. Mixture Proportions and Density for 1 m^3 of Concrete (Standard, Magnesite, and Hydromagnesite)

Concrete	Substitution (wt.%)	Water (W) (kg)	Cement (C) (kg)	Substitute (S) (kg)	Ratio W/(C+S)	Sand (kg)	Gravels (kg)	Density (kg/m^3)
standard	0	195	335	-	0.58	800	1065	2311 ± 25
magnesite	15	195	284.75	50.25	0.58	800	1065	2286 ± 23
hydromagnesite	15	195	284.75	50.25	0.58	800	1065	2269 ± 14

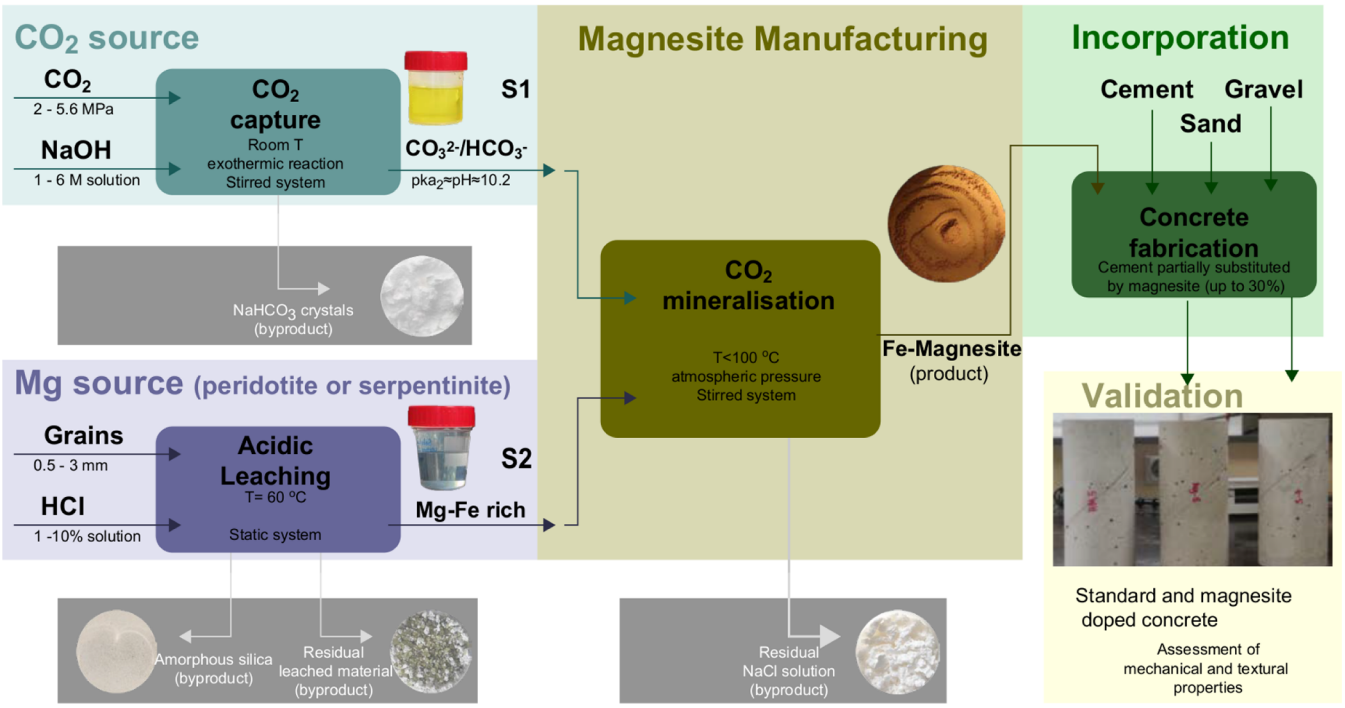

Figure 1. Schematic diagram flow of materials used in three fundamental, interdependent steps for iron-magnesite production, and its use as a partial substitute in concrete fabrication. S1 and S2 indicate the two solutions prepared and mixed to mineralize carbon dioxide and produce an iron-magnesite material that can be used as a partial substitute of cement for the fabrication of concrete.

these experiments were monitored in real-time using Raman spectroscopy, a technique employed to observe the nucleation of various minerals under mild conditions.[8,17−19] Factors such as the alkaline-solution/acidic-solution volume ratio, mixing mode, reaction time, and heat-aging temperature were investigated. Iron-magnesite (500 g) intended for use as a cement substitute in concrete samples was synthesized at 90 °C with a synthesis duration of 24 h in all experiments.

All produced carbonates were recovered by simple settling, and the residual salt-rich solution was naturally evaporated in mini-pools (20 × 20 cm) at ambient temperature to recover the salt (mainly NaCl).

2.4. Ex Situ Characterization of Solutions and Precipitates. Density and ionic concentrations were measured for selected solution samples by using conventional methods. Density was determined by weighing the mass of 100 mL of the solution with a high-precision analytical balance. Concentrations of Mg, Fe, Ca, Al, Si, K, and Na were dosed using ICP-AES. Finally, CO_3^{2-} and HCO_3^- concentrations were determined by Raman spectroscopy.

The solid products were recovered by simple settling and washed twice with tap water in order to remove the soluble salts. They were then dried in air at 60 °C for 24−48 h. The dried solid products were stored in plastic flasks for subsequent characterization of selected samples by Field Emission Gun Scanning Electron Microscopy (FESEM) and powder X-ray diffraction (XRD).

Powder XRD spectra were acquired using a Siemens D5000 diffractometer in Bragg−Brentano geometry, equipped with a theta−theta goniometer with a rotating sample holder. Diffraction patterns were collected using Cu kα_1 ($\lambda_{k\alpha1}$ = 1.5406 Å) and Cu kα_2 ($\lambda_{k\alpha2}$ = 1.5444 Å) radiations in the range 2θ = 10−70°, with a step size of 0.04° and a counting time of 6 s per step. For high-resolution imaging, the solid products were dispersed by ultrasonic treatment in absolute ethanol for 5 min. Two droplets of the suspension were then deposited directly onto an aluminum support and observed without a metal coating to avoid any surface perturbation at high magnification. The powders were imaged using a Zeiss Ultra 55 FESEM with a maximum spatial resolution of approximately 1 nm at 15 kV.

2.5. Materials and Concrete Specimen Preparation. Except for the substitution of 15 wt % Portland cement by magnesite or hydromagnesite, we followed the same procedure for materials and concrete specimen preparation as detailed in other studies.[27,28] The cement used in all mixes was CEM I 52.5 N type Portland cement, meeting the NF EN 197-1 standard.[29] Natural sand and gravel were used as fine and coarse aggregates, respectively. The maximum aggregate size was 3.15 mm for sand and 16 mm for gravel, see ref 27 for the full grading curves. Ordinary tap water was used for mixing and curing. The mass ratio of water to cement + substituent (column W/(C + S) in Table 1) was kept constant at 0.58 for

https://doi.org/10.1021/acs.iecr.5c00744
Ind. Eng. Chem. Res. XXXX, XXX, XXX−XXX

all samples. The concrete without cement substitution can be considered standard concrete.[30]

We prepared 14 concrete samples of each type: standard, cement substituted with 15% magnesite, and cement substituted with 15% hydromagnesite, resulting in a total of 42 specimens. Each concrete specimen was a cylinder with a height h = 140 mm and a diameter φ = 70 mm. All samples for each material were prepared from a single batch. Casting was performed according to the French standard for normal-weight concrete.[30] Following the French norm NF EN 12390-2,[31] the mixtures were poured into cylindrical cardboard molds and compacted using an external vibrating table to achieve consolidation. After casting, the specimens were cured in their cardboard molds in air for 5 days and then submerged in water for 7 days, still within the molds. Afterward, they were demolded and cured into water for an additional 21 days. Finally, they were air-dried for at least 1 day before mechanical measurements were conducted. All mechanical tests were performed after a minimum of 28 days, in accordance with the NF EN 12390-3 standard.[32]

2.6. Texture and Porosity. The visual appearances of three representative samples are shown in Figure 1. Aside from a slightly different color, no significant differences were detected. The density of each sample was measured by weighing, and the average values are reported in Table 1. The magnesite concrete was slightly less dense than the standard concrete, while the hydromagnesite concrete was even less dense. However, the density difference from that of the standard concrete was less than 2%. To compare the texture and the macropore content of the three materials, a representative sample of each material was scanned by using a DeskTom 3D X-ray Computed Tomography (CT) scanner. The macropore size distributions are discussed in the main text.

Synchrotron scans were conducted at beamline BM18 of the European Synchrotron, using an energy of 164 keV and a propagation distance of 6 m for phase contrast optimization. The beam was prefiltered with a 3.75 mm thick molybdenum plate. Helical scans were performed at a 10 μm pixel resolution using an Iris 15 camera and a LuAg2000 scintillator with an exposure time of 40 ms and an accumulation of three exposures (totaling 120 ms). The scans were laterally offset by 2000 pixels to expand the field of view. A total of 15,000 projections per rotation were acquired, yielding 124,051 projections overall.

2.7. Measurement of Elastic Properties of Concrete Samples. The elastic Young's modulus Y (MPa) and the characteristic compressive strength f_{ck} (MPa) are considered fundamental material parameters in the design of concrete structures (e.g., 33). The characteristic compressive strength, f_{ck}, which we discuss in the main text, is used for calculating structures according to the requirements of ultimate limit states, while the elastic Young's modulus, Y, is used to calculate elastic deformations and to design sections of structural concrete elements according to the serviceability limit state.[34] It is generally assumed that Y and f_{ck} are positively correlated, and several different fully empirical (nonlinear) expressions have been proposed to estimate Y from f_{ck} (see, e.g., [35,36] for reviews). However, these expressions may provide reasonable estimates only for specific concrete mixes. Different methods, such as the tangent[35] or secant[34] modulus, have been proposed to directly estimate the so-called static Young's modulus Y_s from the slope of the stress−strain curve in the elastic deformation regime obtained during a uniaxial compression test. However, these methods face challenges in unambiguously defining this elastic regime and accounting for possible nonlinearities at the onset of loading, which are related to geometrical imperfections of the samples or to the elastic stiffness of the loading frame.

For these reasons, and in accordance with the principles of ultrasonic testing described in ASTM C597-02,[37] we employed a nondestructive method, fully detailed elsewhere,[36] based on the measurement of the elastic P-wave velocity V_p, to determine the dynamic modulus Y_d. By placing two piezoelectric transducers-one as the "transmitter" and one as the "receiver"—at both ends of the cylindrical samples, we calculated $V_p$from the travel time Δt of the elastic P-wave through a sample of height h, $V_p = h/\Delta t$. Note that in these ultrasonic measurements, the arrivals of compressive (P) and shear (S) waves are generally indistinguishable. As a result, this method does not allow independent estimation of two elastic constants, such as the dynamic Young's modulus Y_d and the Poisson's ratio ν. However, for normal-weight concrete, data in the literature show no significant dependence of ν on the concrete mix or preparation, with reported values ranging from 0.20 to 0.25.[35,38] Consequently, we assumed a material-independent Poisson's ratio of ν = 0.22, and the dynamic modulus can be obtained from the following equation eq 1:

$$Y_d = V_p^2\left[\frac{\rho(1+\nu)(1-2\nu)}{1-\nu}\right] \quad (1)$$

2.8. Compressive and Characteristic Strength of Concrete Samples. Following the standard,[33] the uniaxial compressive strength of each sample was obtained by applying a constant stress rate of 0.5 MPa/s until failure (see ref 27 for additional details). The corresponding average compressive strength σ_{max} and its standard deviation δ were then calculated for the three sets of 14 samples, for each material, see Table 2.

Table 2. Mechanical Properties of the Three Types of Concrete Produced (N = 14 Samples of Each Type): Standard Concrete, Concrete with 15 wt % Magnesite substitution, and Concrete with 15 wt % Hydromagnesite Substitution

Concrete	Y_d (dynamic Young's modulus), GPa	σ_{max} (average compressive strength), MPa	f_{ck} (characteristic strength), MPa
standard (N = 14)	42.1 ± 2.9	28.5 ± 2.9	23.7
magnesite (N = 14)	38.1 ± 2.9	25.5 ± 1.9	22.4
hydromagnesite (N = 14)	35.2 ± 2.1	21.7 ± 1.2	19.7

The characteristic compressive strength, f_{ck}, used to classify concretes into strength classes for structural design, can be calculated from eq 2:

$$f_{ck} = \sigma_{max} - \lambda\cdot\delta \quad (2)$$

where λ=1.645 for the European standard,[39] and λ=1.34 for the US standard.[33] In the European regulation, this means that the characteristic strength is defined as the strength value below which only 5% of the compression tests are expected to fall, while in the US regulation, a larger tolerance of 10% is allowed, assuming a normal distribution of strengths in both cases. Note that our sample sets (14 samples for each material) were

https://doi.org/10.1021/acs.iecr.5c00744
Ind. Eng. Chem. Res. XXXX, XXX, XXX−XXX

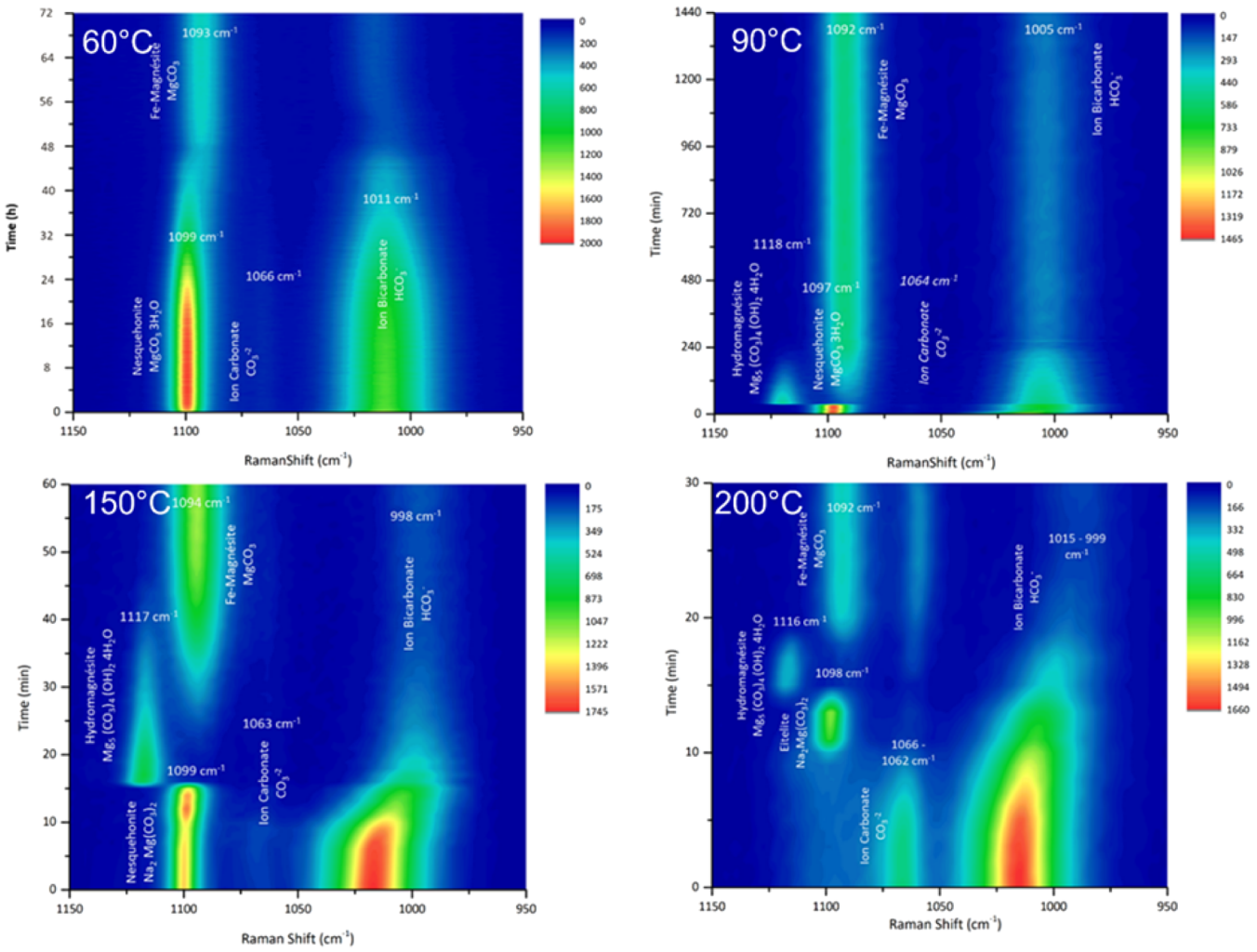

Figure 2. Fe-Magnesite-rich material production at four maturation temperatures (60 and 90 °C (mild conditions) 150 and 200 °C (hydrothermal conditions) through indirect carbonation of peridotite. Kinetics and reaction mechanisms were monitored in real-time using Raman spectroscopy. The time axis concerns times when magnesite (the more stable phase) was reached a spectral equilibration, i.e., that the peak intensity for magnesite is constant and/or reaches a maximum value.

smaller than the recommended size in these standards (e.g., 30 samples for 33).

3. RESULTS AND DISCUSION

3.1. A Novel Circular Flow Material Method for Producing Fe-Magnesite. Previous studies have shown that magnesite can be produced more quickly using commercial magnesium sources, such as fine-powdered brucite ($Mg(OH)_2$) or various soluble Mg-salts, including chloride ($MgCl_2{\cdot}6H_2O$), sulfate ($MgSO_4{\cdot}7H_2O$), nitrate ($Mg(NO_3)_2{\cdot}6H_2O$) and acetate ($Mg(CH_3COO)_2{\cdot}4H_2O$).[8,17−19] In all cases, a temperature of at least 90 °C was required to produce magnesite within a reasonable time frame (1−5 days). High carbonate alkalinity, close to the pK_{a2} of the ionic carbonate speciation, was also a key factor for magnesite production.[17−19] Carbon dioxide pressure does not appear to be a critical parameter in magnesite formation in the investigated systems, except when brucite mineral $Mg(OH)_2$ is used as magnesium source.[8]

Here, we present a novel circular material flow process that consists of three fundamental steps:[1] CO_2 capture in concentrated NaOH solutions, resulting in an alkaline solution (solution S1: HCO_3^-/CO_3^-) and $NaHCO_3$ crystals as byproduct (if NaOH concentration exceeds 4 M).[2] Leaching of Mg−Fe-rich peridotite in concentrated HCl solution (up to 10%), producing an acidic solution enriched in Mg and Fe divalent ions (solution S2), amorphous silica (as a byproduct) and residual leached material.[3] Mineralization of CO_2 (carbonate precipitation) was achieved by mixing solutions S1 and S2. In this precipitation step several carbonate minerals mixed with iron oxides can be produced by a simple heat-aging step from room T to 200 °C. Figure 1 illustrates this circular material flow process, including also the Fe-magnesite utilization as a partial substitute of cement in concrete. The more relevant fundamental results are described below and all steps are commented in the following subsections.

As discussed below, one notable result is the fabrication of iron-magnesite at 60 °C in just 2−4 days. Using real-time Raman spectroscopy, we monitored the direct transformation of nesquehonite into iron-magnesite (Figure 2, top plot on the left). Conversely, a hydromagnesite transient phase (e.g., 8) was also observed at 60 °C under the investigated conditions. This is the most significant result because magnesite formation at low T (≤60) has been reported, but additives and/or catalysts (in vitro and/or in living systems) have systematically used.[20−22] Moreover, several days or weeks are generally

https://doi.org/10.1021/acs.iecr.5c00744
Ind. Eng. Chem. Res. XXXX, XXX, XXX−XXX

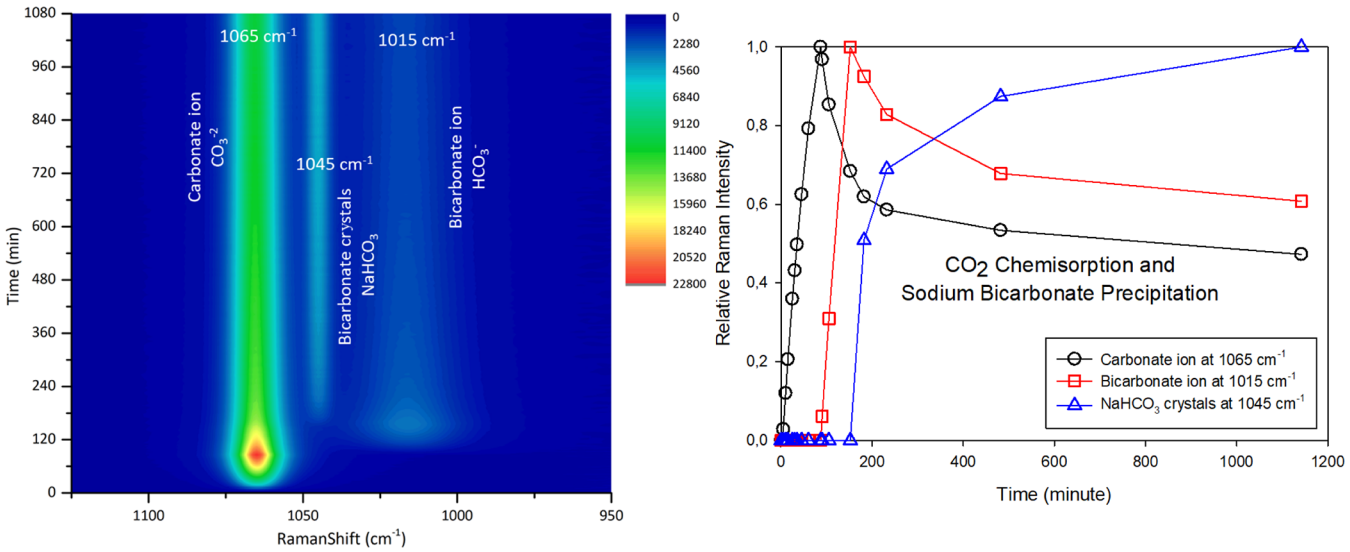

Figure 3. Time-lapse Raman spectroscopy monitoring of CO_2 capture by chemisorption in concentrated NaOH solution (4 M) under anisobaric conditions. Left: Continuous evolution of the carbonate concentrations of the different species over time. Right: Kinetic behavior of carbonate ions and sodium bicarbonate precipitation including only spectra at different time points.

required and the proofs provided for magnesite crystals formation at room temperature are not convincing.[20−22] At higher temperatures, the hydromagnesite transient phase was systematically detected at 90, 150, and 200 °C (Figure 2). As expected, magnesite production time significantly decreased at higher temperatures, with only 90 min required at 150 °C.

In practice, this method utilizes standard and abundant reactants (Mg silicates, water, NaOH, HCl, and CO_2). Additionally, all byproducts ($NaHCO_3$ crystals, amorphous silica nanoparticles, NaCl-rich material, and unreacted silicate grains) and products (nesquehonite, hydromagnesite, magnesite, and carbonate-iron oxide composites) have well-established industrial applications. Furthermore, the permanent storage of industrially captured CO_2 as highly stable iron-magnesite is promising, as this mineral can replace up to 15 wt % fresh cement in concrete fabrication without significantly affecting concrete's porosity or mechanical properties. Currently, the Technology Readiness Level (TRL) for our process is close to TRL 2. In effect, maturating technological studies on the optimization concerning the magnesite fabrication and its use and its extent application to other Mg sources are still required to reach an expected TRL 4. In parallel to maturating studies, an overall life cycle assessment (LCA) and a techno-economic assessment (TEA) on the magnesite production and its use in concrete manufacturing will be required in a near future. In the present study, basic technological research is mainly reported for each step of process, i.e., that LCA and TEA studies are not relevant.

3.2. CO_2 Capture Step. CO_2 capture from industrial sources does not present a significant technological or scientific barrier; however existing methods and technologies, including the recovery of high purity CO_2 and its liquefaction, remain expensive.[40−43] Therefore, improving and optimizing CO_2 capture units still pose important challenges. In this study, we propose the capture of CO_2 by chemisorption in a concentrated NaOH solutions. While this chemical approach involves well-understood reactions, NaOH solution have not, to our knowledge, been widely suggested for capturing carbon dioxide from industrial sources. This may be because CO_2 is primarily captured in ionic form (as rich-carbonate CO_3^{2-}/HCO_3^- solution) and, under specific precipitating conditions, also in crystalline form as $NaHCO_3$. Conversely, NaOH microdrop solutions have been suggested to remove/capture CO_2 from atmospheric air.[44−46]

The advantage of using NaOH solutions for capturing industrial CO_2 is that the resulting ionic carbonate solutions can be easily manipulated, stored in conventional tanks, and used to form stable carbonates, as proposed in this study. Additionally, NaOH solutions are strongly selective for CO_2; the accompanying gases from combustion processes (e.g., NOx, SOx, N_2...) have little or no influence on the CO_2 chemisorption reactions. In the present study, we conducted several CO_2 capture experiments using concentrated NaOH solutions under different conditions, varying mainly the CO_2 injection mode (anisobaric and isobaric), initial gas pressure (from 5 to 55 bar), and NaOH concentration (1−6 M). In all cases, the ionic carbonate concentration and speciation can be determined by using Raman spectroscopy in real time. For example, time-resolved Raman spectroscopy was then employed to monitor the reaction mechanism and kinetics (Figure 3). Our results indicate that the injected CO_2 is rapidly chemisorbed as carbonate ions (main Raman signature at 1065 cm^{-1}) according to the following reaction (Reaction 1):

$$CO_{2(aq)} + 2OH^- \rightarrow CO_3^{-2} + H_2O \quad (chemisorption) \qquad (3)$$

For example, a rapid chemisorption phase reaches its maximum (spectral equilibration) within the first 70 min (Figure 3). Afterward, the chemisorption process involves additional concurrent reactions, during which some of the carbonate ions are partially protonated, leading to the formation of bicarbonate ions (Raman peak at 1015 cm^{-1}). The direct transformation of aqueous carbon dioxide is also expected, introducing protons in the system. This second chemisorption regime can be quickly followed by the precipitation of $NaHCO_3$ crystals (Raman peak at 1045 cm^{-1}), depending on the initial concentration of the NaOH solution ([NaOH] > 4M). All these reaction events monitored in real time by Raman spectroscopy, can be summarized by the following reactions (Reactions 2 to 4):

https://doi.org/10.1021/acs.iecr.5c00744
Ind. Eng. Chem. Res. XXXX, XXX, XXX−XXX

$$CO_{2(aq)} + OH^- \rightarrow HCO_3^- \ (chemisorption) \quad (4)$$

$$CO_3^{-2} + H^+ \rightarrow HCO_3^- \ (protonation) \quad (5)$$

$$HCO_3^- + Na^+ \rightarrow NaHCO_3 \ (crystals\ precipitation) \quad (6)$$

In summary, this CO_2 capture method enables the production of an alkaline carbonate solution where the carbonate/bicarbonate ratio and $NaHCO_3$ formation can be controlled by adjusting the NaOH concentration and the carbon dioxide injection pressure. Additionally, this system does not require high-pressure equipment because all of the above reactions take place from 5 bar of carbon dioxide pressure and all injected CO_2 is completely chemisorbed. Herein, the monitoring in real time by Raman spectroscopy provide clearly the reaction mechanism and kinetics during carbon dioxide capture process by chemisorption reactions. However, this capture step should be tested using more realistic hot gas stream containing carbon dioxide.

3.3. Acid Leaching Step. A Mg-rich solution is produced by acid leaching of Mg-rich minerals, such as olivine from peridotite. The density and ionic concentration of the recovered solutions for a given magnesium source are strongly dependent on the temperature and duration of leaching in the investigated nonstirred experiments. For peridotite material (millimetric grains; 0.5 < size grain < 5 mm), optimal Mg concentrations were achieved when the acidic leaching was conducted at 60 °C for 5−6 days. A hyperbolic empirical model, $\Delta P = (a.t/(b + t)$, describes the behavior of the increase of ionic concentration, $\Delta P = P_i - P_0$, with leaching time t (Figure 4). This simple measurement/analysis provides an overall ionic enrichment of the solution as a function of leaching time until a saturation state at a fixed solid/liquid ratio and at a given acid concentration. However, similar experiments and calculations would be necessary if parameters such as grain size, mineral composition, acid concentration, solid/solution ratio, and temperature are varied.

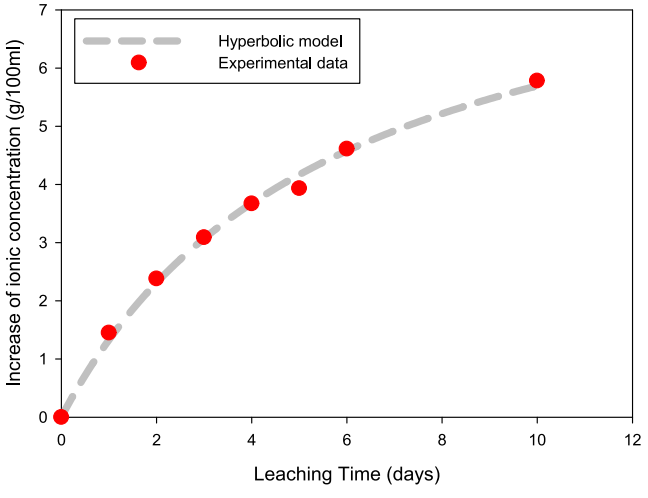

Figure 4. Increase in ionic concentration ($\Delta P = P_i - P_0$ in g/100 mL) for the leaching solution over time at 60 °C and using peridotite grains (0.6 mm < size < 3 mm). P_0 represents the ionic concentration for HCl at 10% and P_i represents the ionic concentration of the leaching solution as a function of time. In all experiments, an amorphous SiO_2 byproduct was also recovered (see also Figure 1).

The high ionic concentrations in leaching solutions after 5 days of reaction were also determined by ICP-AES. Mg was present at 22 g/L and Fe at 4.7 g/L when peridotite millimetric grains were used. Conversely, a more complex ionic solution was obtained using basalt-rich material. In this case, only 7.6 g/L of Mg was leached, but the solution also contained other ions such as Al (5.2 g/L), Fe (5.12 g/L), Na (3.6 g/L), Ca (1.4 g/L), and K (0.64 g/L). Si concentration for both cases is slight ([Si]<110 ppm) because amorphous silica is mainly formed during leaching process. Therefore, iron-magnesite is preferentially fabricated when peridotite grains are used in the leaching step. However, other minerals and mineral composites with potential industrial value can be produced when peridotite, basalt and/or serpentinite grains are used, such as layered double hydroxides, magnetite-magnesite, and/or hematite-magnesite composites (Figure SI-1), whether specific temperature and ionic concentration are controlled. In practice, all leaching experiments using peridotite, basalt and serpentinite produced amorphous silica. This byproduct material has several industrial applications, including in microelectronics, chromatography, semiconductors, and as mineral additive or filler. Additionally, the recovered residual leached material could be reused in subsequent leaching cycles. At an industrial scale, millimetric leached-peridotite grains could also serve as a sand substitute (due to their similar grain sizes) in concrete fabrication and other construction materials. Obviously, all these circular uses possibilities remain to be assessed in the near future, but conceptually all generated solids and solutions can be used and/or reused as illustrated in Figure 1.

In this first study, peridotite was chosen due to its abundant natural availability and high Mg content. However, serpentinite and basalt materials are also suitable candidates for obtaining Mg−Fe-rich solutions to produce stable anhydrous carbonates and mineral composites. Additionally, several other sources containing divalent cations (Mg, Fe and Ca), excepting carbonates, can be used, such as mine wastes, steel slags, asbestos wastes, paper mill wastes, gypsum (raw or waste), and industrial brines.[7,13,47,48] This means that additional exploratory and maturation studies using different divalent-cation sources are required to advance this circular flow material process. In the present study, we focus exclusively on the formation of iron-magnesite from peridotite because magnesite is an enigmatic challenging mineral, as described in the introduction.

3.4. Iron-Magnesite Fabrication by Indirect Carbonation of Peridotite. In our process, the production of iron-magnesite is highly dependent on the CO_2 capture step as it requires the fabrication of an alkaline solution with a controlled carbonate/bicarbonate ratio and concentrations. The leaching step is also crucial because magnesite amount and the iron content in the structure and as iron oxide adhered particles are directly related to this step. Fabricating magnesite involves then the controlled mixing of the leaching solution (x volume of S1) into alkaline solution (2× volume of S2) at a flow rate from 2 to 12 mL/min and under ambient conditions (room T and without redox control). This approach helps prevent CO_2 degassing (e.g., $HCO_3^- + H^+ = CO_2 + H_2O$) until complete neutralization occurs (see Figures SI-2 and SI-3). Following this, a maturation or a heat-aging step, under mild conditions (60 or 90 °C and atmospheric pressure), is then required to produce iron-magnesite in 2−4 days at 60 °C or in 5−10 h at 90 °C as determined by time-resolved Raman spectroscopy

https://doi.org/10.1021/acs.iecr.5c00744
Ind. Eng. Chem. Res. XXXX, XXX, XXX−XXX

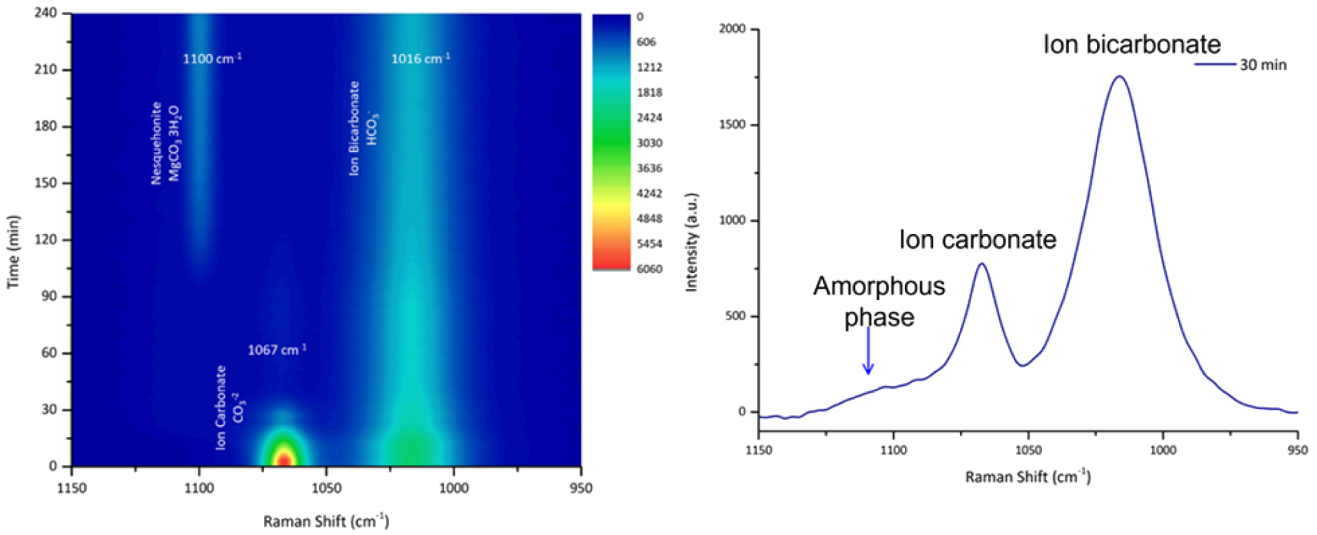

Figure 5. Left: time-lapse Raman spectroscopy monitoring of nesquehonite formation at room temperature, by mixing alkaline and leaching solutions. Right: Raman spectra after 30 min showing the formation of an amorphous carbonate phase prior to the nucleation of nesquehonite.

(see Figure 2). As expected, a higher temperature strongly reduces the time for magnesite production (Figure 2). Energetic requirements and the possibility to use free-carbon energies remains to be examined and refined in an overall context via a carbon footprint analysis, but this was not relevant for this reported basic research, focused mainly on the kinetics and reaction mechanism. For example, the time-resolved Raman spectroscopy measurements (Figure 5) show that an amorphous magnesium or ferrous carbonate phase initially forms before the nucleation of nesquehonite at room temperature. A gelling aspect during solutions mixing step at room T until a solid−liquid separation process agrees with this assumption. Although amorphous or poorly crystallized iron oxyhydroxides are also expected in minor proportion, but they were not detected by Raman spectroscopy. Moreover, the red-brown color and FESEM imagery of the recovered nesquehonite-rich material support this assumption (Figures 6 and SI-2). The relevant chemical precipitation reactions determined from time-resolved Raman spectroscopy and *ex-situ* solid characterization can be simplified for Mg chemistry as follows (Reactions 5 and 6):

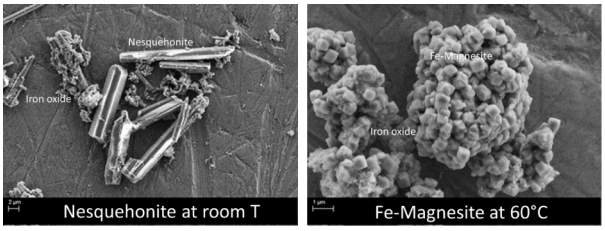

Figure 6. FESEM images showing Nesquehonite and iron-magnesite crystals formed at room temperature and 60 °C, respectively. Both Mg-carbonate minerals mixed with iron oxyhydroxide nanoparticles adhered to carbonate crystals (in minor proportions), providing yellow-red-brown coloration of powdered recovered materials. Iron oxyhydroxide nanoparticles were not detected by in situ Raman spectroscopy or by laboratory X-ray diffraction, but their presence was clearly identified by FESEM imagery and local EDS analyses.

$$Mg^{2+} + CO_3^{-2} + (x+3)H_2O \rightarrow MgCO_3\cdot(x+3)H_2O \quad (AMC\ formation) \tag{7}$$

$$MgCO_3\cdot(x+3)H_2O \rightarrow MgCO_3\cdot 3H_2O + xH_2O \quad (nesquehonite\ formation) \tag{8}$$

Ferrous iron ions can also incorporate into the carbonate phases and/or partially oxidize to form ferric iron phases, since the ionic mixtures were not isolated from the atmosphere and the redox conditions were not systematically controlled in the closed reactors. Consequently, only nesquehonite mixed with minor amounts of iron phases were obtained at room temperature (Figure 6, FESEM image on the left). The production of magnesite requires a higher temperature ($T \geq 60$ °C), as shown in Figure 2. Interestingly, time-resolved Raman spectroscopy measurements have revealed two different reaction pathways for magnesite formation.

First, a direct transformation of nesquehonite into magnesite at 60 °C is illustrated in Figure 2 (top plot on the left) and summarized by the following overall reaction (Reaction 7):

$$MgCO_3\cdot 3H_2O + xFe^{2+} \rightarrow Mg_{1-x}Fe_xCO_3 + xMg^{2+} + 3H_2O \quad (Fe\text{-}magnesite\ formation) \tag{9}$$

Here, the intensity of the bicarbonate ion signature decreases significantly with time, indicating that the transformation of nesquehonite into magnesite is also accompanied by an additional carbonation of residual dissolved ions and the incorporation of ferrous iron, as qualitatively evidenced by a shift in lattice vibration modes from 330 until 323 cm^{-1} for magnesite at 60 °C (330 cm^{-1} correspond to a typical peak for high-purity magnesite crystals). This suggests a partial dissolution-recrystallization pathway. The recovered iron-magnesite was characterized by submicrometric rhombohedral crystals mixed with iron oxyhydroxide nanoparticles (Figure 6, FESEM image on the right). X-ray diffraction and EDS chemical analyses (see Figures SI-4 and SI-5) of the magnesite crystals also suggest some structural incorporation of Fe(II) because a shift of reflection peaks was also detected (Figure SI-5), indicating a partial substitution of Mg by Fe(II) in

https://doi.org/10.1021/acs.iecr.5c00744
Ind. Eng. Chem. Res. XXXX, XXX, XXX−XXX

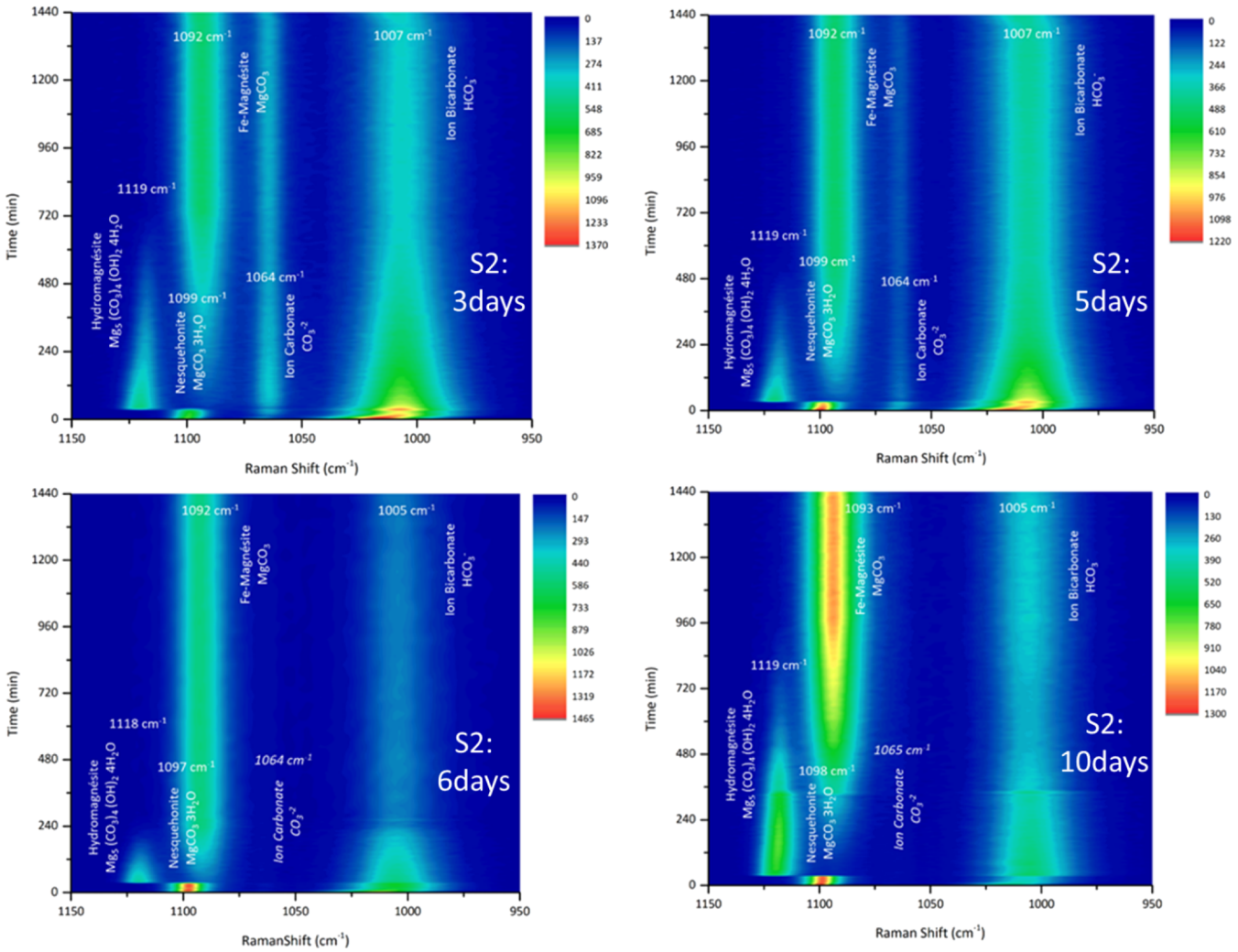

Figure 7. Fe-Magnesite-rich material production at 90 °C for four different concentrations of ionic solution (solution S2 (Figure 1) as a function of leached time (see also Figure 4)), i.e., solutions leached for 3, 5, 6, and 10 days respectively. Kinetics and reaction mechanisms were monitored in real-time using Raman spectroscopy (see also kinetic indicators summarized in Table 1). The time axis was constrained at 24 h (1440 min) and this time is enough to produce magnesite at 90 °C (the more stable phase). In all cases, magnesite was reached a spectral equilibration, i.e., that the peak intensity for magnesite is constant and/or reaches a maximum value.

Table 3. Summary of Kinetic Indicators Determined from Time-Resolved Raman Spectroscopy Measurements for Transient Phases and Magnesite Nucleation Until Spectral Equilibration at 90°C[a,b]

	Leaching Time (day)							
Kinetic indicator (minute)	1	2	3+	3*	4	5+	6+	10+
Nesquehonite persistence	51	30	50	38	148	35	45	36
Hydromagnesite nucleation	21	25	37	30	38	28	32	34
Hydromagnesite persistence	1446	1040	1077	661	503	421	240	780
Fe-Magnesite nucleation++	566	260	177	121	148	121	100	120
Fe-magnesite equilibration	>1446	1360	1317	841	923	576	375	1080

[a]Ionic solutions were obtained by leaching of peridotite millimetric grains from 1 to 10 days at 60°c (ionic concentration was reported in Figure 4). [b]*: replica; + : spectral behavior reported in Figure 7; ++: concern the detection time of lattice mode at 330 cm^{-1} characteristic for magnesite crystals; Nesquehonite peaking at 1098−1100 cm^{1}; Hydromagnesite peaking at 1117−1119 cm^{-1}.

magnesite crystals, as summarized in reaction 7. In summary, the magnesite production at 60 °C via a direct transformation of nesquehonite in only 2 days is the most important scientific result because this insight has not been reported in the literature to the best of our knowledge. Some studies have reported magnesite formation at lower temperature in biotic systems and/or in vitro using organic catalysts, but, several days or weeks were required.[20−22]

Second, the more common transformation of nesquehonite to magnesite involves hydromagnesite ($Mg_5(CO_3)_4(OH)_2 \cdot 4H_2O$) as a transient phase, as previously described.[8] In this study, the transformation from hydromagnesite to magnesite also involves the incorporation of iron into the magnesite

https://doi.org/10.1021/acs.iecr.5c00744
Ind. Eng. Chem. Res. XXXX, XXX, XXX−XXX

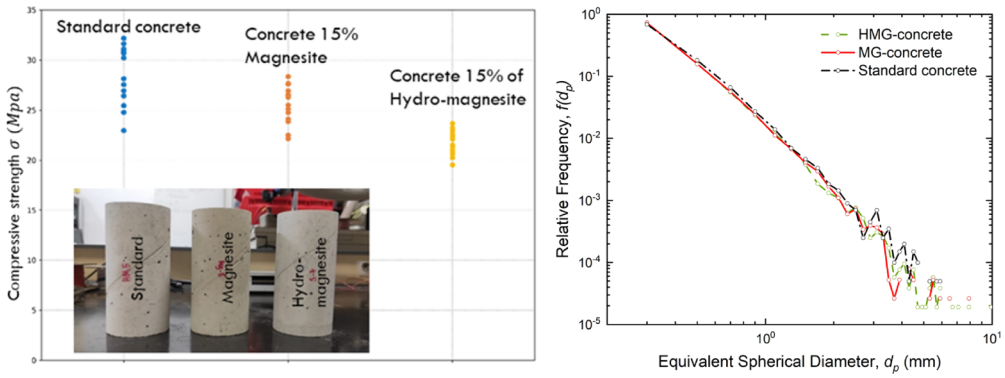

Figure 8. Compressive strength (left) and pore sizes distributions (densities of probability), for the three concretes: Standard concrete, Magnesite-concrete, and Hydromagnesite-concrete. On the left figure, each colored dot corresponds to the strength of one individual compression test. The inset shows the visual appearance of virgin concrete samples (before mechanical loading). On the right figure, the pore sizes are expressed in terms of equivalent spherical diameters.

structure, as summarized by the following overall reaction (Reaction 8):

$$Mg_5(CO_3)_4(OH)_2{\cdot}4H_2O + HCO_3^- + 5xFe^{2+} \rightarrow 5Mg_{1-x}Fe_xCO_3 + 5xMg^{2+} + 5H_2O + OH^- \quad (Fe\text{-}magnesite\ formation) \quad (10)$$

The dissolution-recrystallization pathway is also observed at higher temperatures. However, when hydromagnesite forms at 60 °C (in 25% of the experiments), it slows the overall nesquehonite-to-magnesite transformation, which lasts for 2−3 days. In fact, hydromagnesite is a more stable phase than nesquehonite as clearly demonstrated in ref 49. In contrast, at higher temperatures (90, 150, and 200 °C), the hydromagnesite transient-phase has a reduced impact on the nesquehonite-to-magnesite transformation. At these higher temperatures, the persistence of hydromagnesite is limited to several minutes at 150 and 200 °C and several hours at 90 °C (Figure 2). In the present study, 90 °C seems to be the more promising because it remains a moderate temperature and the formation kinetics of magnesite is less than 24 h. Moreover, the magnesite formation mechanism at 90 °C is independent of the ionic Mg−Fe concentration (or leaching time), as illustrated in Figure 7. This means that in all cases magnesite is formed via hydromagnesite transient phase and only nucleation and persistence time (or lifetime) of transient phases are impacted as summarized in Figure 7 and Table 3.

In summary, magnesite can be produced from the indirect carbonation of peridotite by mixing two ionic solutions and heating the resulting suspensions at mild temperature and atmospheric pressure (60 and 90 °C; see Figures 2 and 7). As expected, the production time for iron-magnesite decreases significantly with increasing temperature, as illustrated in Figure 2, from several days to just minutes (spectral Raman equilibration in real-time). For instance, producing iron-magnesite at 90 °C from indirect carbonation of peridotite could be a promising technology for pilot and industrial scales, as it requires only 5−6 h to produce iron-magnesite from ionic solutions (Figure 7). Herein, the amorphous phase and nesquehonite formed at ambient conditions are rapidly transformed into a hydromagnesite transient phase, which has only a slight impact on iron-magnesite formation due to its short lifetimes (Figure 7 and Table 3). In a scientific context, the magnesite formation from direct transformation of nesquehonite at 60 °C remains the most important insight as invoked above. Then, these results are significant because high quantities of magnesite can be produced at moderate temperatures in reasonable times—2−4 days at 60 °C and only 5−6 h at 90 °C. The fabrication time of magnesite decreases sharply with temperature, requiring only 90 min at 150 °C and less than 60 min at 200 °C (Figure 2). It is important to note that the effectiveness of these mild conditions for magnesite production was probably influenced by the presence of competitive cations in the system, specifically Fe(II) and, to a lesser extent, Ca. The role of divalent cations in magnesite formation kinetics has been demonstrated recently, particularly regarding the influence of calcium during Ca-magnesite formation at 90 °C.[19]

3.5. Utilization of Iron-Magnesite as a Partial Substitute of Cement. We used iron-magnesite material produced at 90 °C from indirect carbonation of peridotite as a 15 wt % substitute for cement (Figure 1). In the cement industry, this substitution could reduce clinker production and securely store CO_2 within the material, minimizing the risk of re-emission during the concrete's lifespan or when reused as aggregate for concrete recycling.[50] A key concern is ensuring that this substitution does not significantly affect the mechanical and textural properties of the concrete. To address this, we tested concrete samples with substituted cement with both iron-magnesite synthesized at 90 °C from indirect carbonation of peridotite (this study), and hydromagnesite synthesized at 60 °C from direct carbonation of brucite following the method described in.[8] We prepared cylindrical concrete samples (7 cm in diameter and 14 cm high) with either iron-magnesite or hydromagnesite as a partial substitute for Portland cement. We assessed these materials in terms of internal texture and porosity using X-ray tomography imaging as well as elastic stiffness (Young's modulus) and compressive strength. The standard concrete for its casting presents a ratio of W/(C + S) equal at 0.58 (see Table 1). This ratio leads a concrete C20/25 i.e., a concrete which have a characteristic strength (f_{ck}) equal to 20 MPa after 28 days of curation.[26,50] The compressive strength results for the three types of concrete are summarized in Table 2, using the European standard) λ = 1.645, see Supporting Information). We observed a slight decrease in strength of 1.3 MPa (5.5%) for magnesite concrete and a more notable decrease for hydromagnesite concrete (4 MPa, or 16.9%). The greater reduction in strength for hydromagnesite concrete is expected as the

https://doi.org/10.1021/acs.iecr.5c00744
Ind. Eng. Chem. Res. XXXX, XXX, XXX−XXX

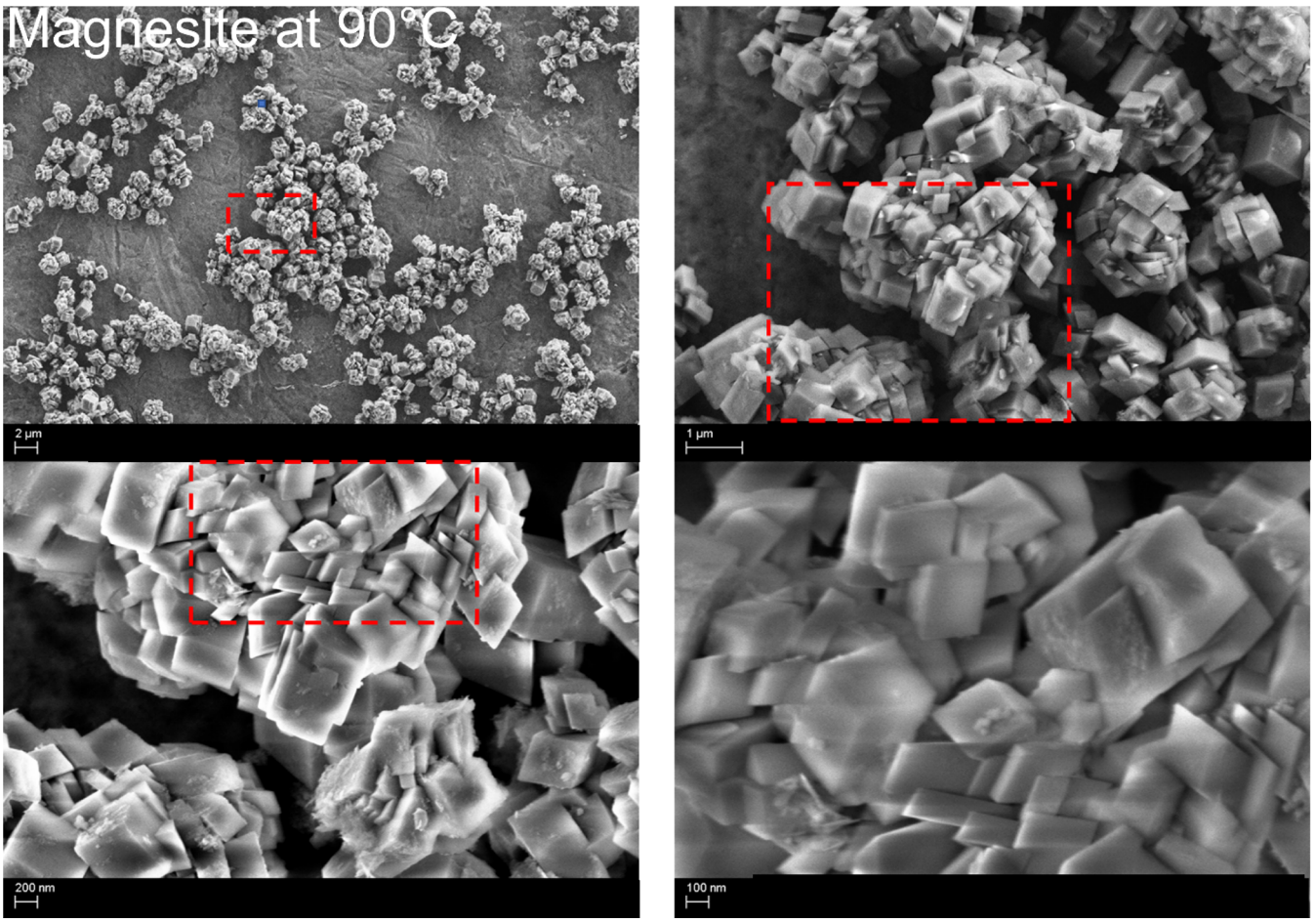

Figure 9. FESEM images at four different magnifications for Fe-magnesite produced at 90 °C from indirect carbonation of peridotite. Millimetric grains of peridotite leached 5 days at 60 °C under in a static system (without stirring). Kinetics and reaction mechanism was also reported in Figure 7.

introduction of hydromagnesite increases the total water content of the cement paste. The results for magnesite concrete are promising (Figure 8). However, these assessments are preliminary. Strength differences might be reduced with optimization of the mix (water, sand, gravels) or the preparation process. Further work could involve exploring the mechanical properties of the cements at scales ranging from the nanometer-sized particles of calcium-silicate-hydrate (C−S−H) to the size of the magnesite microparticles and/or microaggregates (see Figure 9) using techniques such as nano- and microindentation.[51] Additionally, the rheology of fresh concrete pastes[52] was not analyzed, as we focused only on the mechanical properties of hardened concrete samples. Lastly, due to the limited amount of magnesite or hydromagnesite synthesized at the laboratory scale, we tested only 14 samples of each material—fewer than the recommended 30 samples for accurately estimating characteristic concrete strength according to regulatory codes.[30]

One sample of each concrete type was scanned before deformation using a DeskTom 3D X-ray Computed Tomography (CT) scanner at a resolution of 50 μm and after deformation at the BM18 beamline at the European Synchrotron Radiation Facility with a voxel size of 10 μm using propagation phase-contrast. The raw X-ray images were segmented to identify pores, but only those larger than 3 × 3 × 3 voxels were considered meaningful. Thus, these tomographic analyses capture only macropores and micropores and do not resolve nanoporosities present in the hardened cement paste (e.g., 26, 50).

From the reconstructed 3D pore structures, no significant differences in texture were detected. The pore size distributions before deformation, expressed in terms of equivalent spherical diameters (d_p) are shown in Figure 8 (plot on the right). These distributions follow a power-law trend $f(d_p) \sim d_p^{-\alpha_p}$ with $\sigma_p \simeq 3.3$. The only detectable difference is the presence of a few larger pores ($6\ mm \leq d_p \leq 10\ mm$) in magnesite- and hydromagnesite concrete, which are absent in standard concrete. Consequently, macroporosity (p) is slightly higher in magnesite concrete (p = 1.25%) and hydromagnesite concrete (p = 1.69%) compared to the standard concrete (p = 0.86%). These differences are relatively small and may not fully represent all samples but are consistent with minor differences in density noted previously. In addition, macro-porosity seems to be slightly affected after deformation into no-fractured zones as illustrated from tomographic synchrotron measurements (Figure 10). Herein, macropores and fractures were reconstructed at higher resolution on the BM18 beamline offering a powerful tool to determine a textural impact in doped concretes.

Eight elastic velocity measurements were performed on each type of concrete sample, with the results reported in Table 3. The dynamic Young's modulus decreased by approximately

https://doi.org/10.1021/acs.iecr.5c00744
Ind. Eng. Chem. Res. XXXX, XXX, XXX−XXX

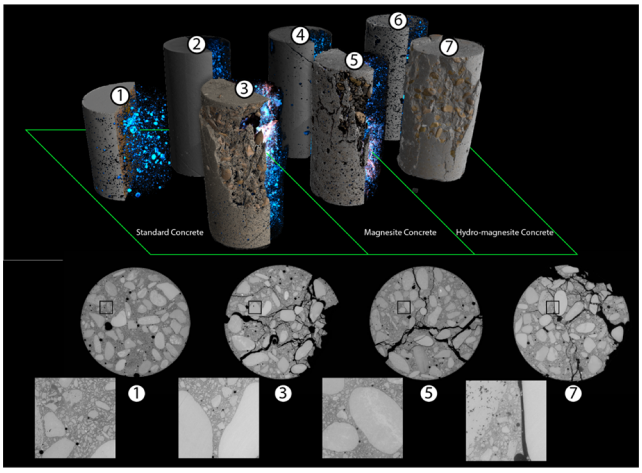

Figure 10. Tomographic analysis of standard, magnesite, and hydro-magnesite concretes. The images labeled 1, 2, 4, and 6 show the samples before testing deformation, while those labeled 3, 5, and 7 display the samples after failure. The top section presents 3D volume rendering with transparency to highlight pores (blue) and cracks (red). The bottom section shows the middle slice of samples 1, 3, 5, and 7, including a zoomed-in view. Porosity is indicated by black regions, and the cement phase in shown in gray.

9.5% for magnesite concrete and 16% for hydromagnesite concrete, compared to standard concrete. The observed decrease in magnesite concrete cannot be explained by a simple mixing law for composite materials, as the Young's modulus of bulk magnesite at room temperature and atmospheric pressure is 174 GPa, significantly higher than the typical values for consolidated cement (~10−30 GPa).

This reduction cannot be easily explained by the small differences of (macro) porosities noted earlier. Classical models relating the Young's modulus Y to porosity p, such as $Y(p) = Y_0(1 - \frac{p}{p_c})^{\alpha}$, where Y_0 is the Young's modulus of the bulk (pore-free) material and p_c is the porosity at which the Young's modulus vanishes,[53] suggest only a minor decrease in elastic stiffness. For standard concrete, with $\sigma = 1$ and $p_c \approx 42\%$, this model reasonably fits experimental data.[54] Based on the measured porosities, the model predicts a decrease in elastic stiffness of less than 1% for magnesite concrete and about 2% for hydromagnesite concrete. Therefore, the observed elastic softening is likely due to the structure of the hardened cement containing magnesite or hydromagnesite particles, including the specific structure and interactions of these particles within the cement matrix. Future analyses, such as nano- and microindentation measurements, will be essential to further explore these structural effects and their impact on mechanical properties.

4. CONCLUSION

The present study introduces a circular flow material method for producing iron-magnesite via indirect carbonation of peridotite. Conducted on a laboratory scale with liter-volume capacity, this method efficiently generates iron-magnesite under mild ($T \leq 90$ °C) and hydrothermal (up to 200 °C) conditions within a time scale coherent for industrial processes (from h to days). In practice, the process offers significant potential for high-use applications and provides a mechanism for permanently storing industrially captured CO_2. Our preliminary analysis suggests that the partial substitution of cement with magnesite particles could notably reduce the carbon footprint of the cement on concrete industry. Evaluations reveal only marginal differences in density, porosity, or texture between hardened magnesite concrete and standard concrete. Additionally, the observed degradation of mechanical properties, such as Young's modulus and characteristic strength, is minimal. These findings support the viability of iron-magnesite material as a promising sustainable alternative in concrete production.

In a scientific context, this study reports for the first time that the magnesite "an enigmatic mineral in geology" can be significantly produced at 60 °C and atmospheric pressure via a direct transformation of nesquehonite into magnesite; this chemical-mineral transformation was then monitored in real time by Raman spectroscopy. Obviously, these results open new possibilities to investigate on the nucleation of "enigmatic" anhydrous magnesium carbonates such as magnesite, dolomite, huntite, and ankerite debated in the last two centuries.

■ ASSOCIATED CONTENT

Data Availability Statement

All data needed to evaluate the conclusions in the paper are present in the paper and/or the Supporting Information.

Supporting Information

The Supporting Information is available free of charge at https://pubs.acs.org/doi/10.1021/acs.iecr.5c00744.

Figures SI-1 to SI-5 concerning FESEM images, X-ray diffraction patterns, pH titration, and some photographs for selected experiments (PDF)

■ AUTHOR INFORMATION

Corresponding Author

German Montes-Hernandez − *ISTerre, Univ. Grenoble Alpes, Grenoble INP, Univ. Savoie Mont Blanc, CNRS, IRD, Univ. Gustave Eiffel, Grenoble 38000, France;* orcid.org/0000-0002-6692-3903; Email: german.montes-hernandez@univ-grenoble-alpes.fr

Authors

Jérôme Weiss − *ISTerre, Univ. Grenoble Alpes, Grenoble INP, Univ. Savoie Mont Blanc, CNRS, IRD, Univ. Gustave Eiffel, Grenoble 38000, France*

Sarah Clavier − *ISTerre, Univ. Grenoble Alpes, Grenoble INP, Univ. Savoie Mont Blanc, CNRS, IRD, Univ. Gustave Eiffel, Grenoble 38000, France*

Benoît Cordonnier − *The European Synchrotron Radiation Facility (ESRF), Grenoble 38000, France*

Paul Tafforeau − *The European Synchrotron Radiation Facility (ESRF), Grenoble 38000, France*

Olivier Plé − *Université Savoie Mont Blanc, CNRS, LOCIE, Chambéry 73000, France*

François Renard − *ISTerre, Univ. Grenoble Alpes, Grenoble INP, Univ. Savoie Mont Blanc, CNRS, IRD, Univ. Gustave Eiffel, Grenoble 38000, France; The Njord Centre, Department of Geosciences and Physics, University of Oslo, Oslo 0316, Norway*

Complete contact information is available at: https://pubs.acs.org/10.1021/acs.iecr.5c00744

Notes

The authors declare no competing financial interest.

https://doi.org/10.1021/acs.iecr.5c00744
Ind. Eng. Chem. Res. XXXX, XXX, XXX−XXX

■ ACKNOWLEDGMENTS

The authors acknowledge funding from the French National Centre for Scientific Research (exploratory project PEPS-CNRS 2023 and multidisciplinary project MITI-CNRS "Ressources et Sobriété" 2024-2025), the Université Grenoble Alpes (BQR-ISTerre 2022), the European Synchrotron Radiation Facility BM18 beamline for in-house beamtime access, and the European Union Horizon 2020 program (Accelerating CCS Technologies, project FUNMIN No. 294766).

■ REFERENCES

(1) *Intergovernmental Panel On Climate Change (IPCC)*, 2023. https://www.ipcc.ch/report/sixth-assessment-report-cycle/.
(2) Habert, G.; Miller, S. A.; John, V. M.; Provis, J. L.; Favier, A.; Horvath, A.; Scrivener, K. Environmental impacts and decarbonization strategies in the cement and concrete industries. *Nat. Rev. Earth Environ.* **2020**, *1*, 559−573.
(3) Miller, S. A.; John, V. M.; Pacca, S. A.; Horvath, A. Carbon dioxide reduction potential in the global cement industry by 2050. *Cem. Concr. Res.* **2018**, *114*, 115−124.
(4) Barbhuiyaa, S.; Kanavaris, F.; Bhusan Das, B.; Idrees, M. Decarbonising cement and concrete production: Strategies, challenges and pathways for sustainable development. *J. Build. Eng.* **2024**, *86*, 108861.
(5) Cavalett, O.; Watanabe, M. D.; Voldsund, M.; Roussanaly, S.; Cherubini, F. Paving the way for sustainable decarbonization of the European cement industry. *Nat. Sustain.* **2024**, *7* (5), 568−580.
(6) Pisciotta, M.; Pilorgé, H.; Davids, J.; Psarras, P. Opportunities for cement decarbonization. *Clean. Eng. Technol.* **2023**, *15*, 100667.
(7) Montes-Hernandez, G.; Perez-Lopez, R.; Renard, F.; Nieto, J. M.; Charlet, L. Mineral sequestration of CO2 by aqueous carbonation of coal combustion fly-ash. *J. Hazardous Mater.* **2009**, *161*, 1347−1354.
(8) Montes-Hernandez, G.; Bah, M.; Renard, F. Mechanism of the formation of engineered magnesite: A useful mineral to mitigate CO2 industrial emissions. *J. CO2 Util.* **2020**, *35*, 272−276.
(9) Saravanan, A.; Senthil Kumar, P.; Vo, D.-V. N.; Jeevanantham, S.; Bhuvaneswari, V.; Narayanan, V. A.; Yaashikaa, P. R.; Swetha, S.; Reshma, B. A comprehensive review on different approaches for CO2 utilization and conversion pathways. *Chem. Eng. Sci.* **2021**, *236*, 116515.
(10) Pan, S. Y.; Chen, Y. H.; Fan, L. S.; Kim, H.; Gao, X.; Ling, T. C.; Chiang, P. C.; Pei, S. L.; Gu, G. CO2 mineralization and utilization by alkaline solid wastes for potential carbon reduction. *Nat. Sustain.* **2020**, *3*, 399−405.
(11) Chang, M.; Thellufsen, J. Z.; Zakeri, B.; Pickering, B.; Pfenninger, S.; Lund, H.; Østergaard, P. A. Trends in tools and approaches for modelling the energy transition. *Appl. Energy* **2021**, *290*, 116731.
(12) Geerlings, H.; Zevenhoven, R. CO2 mineralization—Bridge Between Storage and Utilization of CO2. *Annu. Rev. Chem. Biomol. Eng.* **2013**, *4*, 103−117.
(13) Ho, H.-J.; Iizuka, A.; Shibata, E. Carbon capture and utilization technology without carbon dioxide purification and pressurization: A review on its necessity and available technologies. *Ind. Eng. Chem. Res.* **2019**, *58* (21), 8941−8954.
(14) Ostovari, H.; Müller, L.; Mayer, F.; Bardow, A. A climate-optimal supply chain for CO2 capture, utilization, and storage by mineralization. *J. Cleaner Prod.* **2022**, *360*, 131750.
(15) Fu, L.; Ren, Z.; Si, W.; Ma, Q.; Huang, W.; Liao, K.; Huang, Z.; Wang, Y.; Li, J.; Xu, P. Research progress on CO2 capture and utilization technology. *J. CO2 Util.* **2022**, *66*, 102260.
(16) Montes-Hernandez, G.; Renard, F.; Chiriac, R.; Findling, N.; Toche, F. Rapid precipitation of magnesite micro-crystals from Mg(OH)2-H2O-CO2 slurry enhanced by NaOH and a heat-ageing step (from 20 to 90°C). *Cryst. Growth Des.* **2012**, *12*, 5233−5240.
(17) Montes-Hernandez, G.; Renard, F. Time-resolved in situ Raman spectroscopy of the nucleation and growth of siderite, magnesite and calcite and their precursors. *Cryst. Growth Des.* **2016**, *16*, 7218−7230.
(18) Montes-Hernandez, G.; Renard, F.; Auzende, A. L.; Findling, N. Amorphous calcium-magnesium carbonate (ACMC) accelerates dolomitization at room temperature under abiotic conditions. *Cryst. Growth Des.* **2020**, *20*, 1434−1441.
(19) Montes-Hernandez, G. Magnesite Formation from Nesquehonite Slurry at 90°C using some Soluble Mg Salts: Eitelite as an Atypical Transient Mineral Phase. *Chem. Eng. Sci.* **2024**, *287*, 119776.
(20) McCutcheon, J.; Power, I. M.; Shuster, J.; Harrison, A. L.; Dipple, G. M.; Southam, G. Carbon Sequestration in Biogenic Magnesite and Other Magnesium Carbonate Minerals. *Environ. Sci. Technol.* **2019**, *53*, 3225−3237.
(21) Hobbs, F. W. C.; Xu, H. Magnesite formation through temperature and pH cycling as a proxy for lagoon and playa paleoenvironments. *Geochem. Cosmochem. Acta* **2020**, *269*, 101−116.
(22) Power, I. M.; Kenward, P. A.; Dipple, G. M.; Raudsepp, M. Room Temperature Magnesite Precipitation. *Cryst. Growth Des.* **2017**, *17*, 5652−5657.
(23) Rak, L.; Beaudoin, J. J.; Mitchell, L. Layered double hydroxide-like materials: Nanocomposites for use in concrete. *Cement Concret. Res.* **2004**, *34*, 1717−1724.
(24) Yang, H.; Xiong, C.; Liu, X.; Liu, A.; Li, T.; Ding, R.; Shah, S. P.; Li, W. Application of layered double hydroxides (LDHs) in corrosion resistance of reinforced concrete-state of the art. *Construc. Build. Mater.* **2021**, *307*, 124991.
(25) Koťátková, J.; Zatloukal, J.; Reiterman, P.; Kolář, K. Concrete and cement composites used for radioactive waste deposition. *J. Environ. Radioact.* **2017**, *178*−*179*, 147−155.
(26) Kastrinakis, A.; Skliros, V.; Tsakiridis, P.; Perraki, M. CO2-mineralised Nesquehonite: A New "Green" Building Material. *Mater. Proc.* **2021**, *5*, 60.
(27) Vu, C.-C.; Weiss, J.; Plé, O.; Amitrano, D.; Vandembroucq, D. Revisiting statistical size effects on compressive failure of heterogeneous materials, with a special focus on concrete. *J. Mech. Phys. Solids* **2018**, *121*, 47−70.
(28) Vu, C. C.; Weiss, J.; Plé, O.; Amitrano, D. Revisiting the concept of characteristic compressive strength of concrete. *Constr. Build. Mater.* **2020**, *263*, 120126.
(29) Association Francaise de Normalisation *NF EN 197−1, Ciment -Partie 1: Composition, spécifications et critères de conformité des ciments courants*, Association Française de Normalisation (AFNOR), 2012.
(30) Association Française de Normalisation (AFNOR) *NF EN 206−1, Béton - Partie 1: Spécification, performances, production et conformité*, Association Française de Normalisation (AFNOR), 2004.
(31) Association Française de Normalisation (AFNOR) *NF EN 12390−2, Essais pour béton durci - Partie 2: Confection et conservation des éprouvettes pour essais de résistance*, Association Française de Normalisation (AFNOR), 2012.
(32) Association Française de Normalisation (AFNOR) *NF EN 12390−3, Essais pour béton durci - Partie 3: Résistance à la compression des éprouvettes*, Association Française de Normalisation (AFNOR), 2019.
(33) Zhou, F. P.; Lydon, F. D.; Barr, B. I. G. Effect of coarse aggregate on elastic modulus and compressive strength of high performance concrete. *Cem. Concr. Res.* **1995**, *25*, 177−186.
(34) ACI Committee *ACI 318−05, Building Code Requirements for Structural Concrete and Commentary*, American Concrete Institute, 2005.
(35) Mehta, P. K.; Monteiro, P. J. M. *Concrete: Microstructure, properties, and materials*, McGraw-Hill Education, 2014.
(36) Vu, C.-C.; Weiss, J.; Plé, O.; Amitrano, D. The potential impact of size effects on compressive strength for the estimation of the Young's modulus of concrete. *Mater. Struct.* **2021**, *54*, 196.
(37) ASTM C597−02. *Standard test method for pulse velocity through concrete*, ASTM International: West Conhohocken, PA, 2002.

https://doi.org/10.1021/acs.iecr.5c00744
Ind. Eng. Chem. Res. XXXX, XXX, XXX−XXX

(38) Neville, A. M.; Brooks, J. J. *Properties of concrete*, 4th ed.; Pearson Education Limited, 2010.
(39) European Committee For Standardization *EN 1992. Eurocode 2: Design Of Concrete Structures − Part 1−1: general Rules And Rules For Buildings*, European Committee For Standardization, 2004
(40) Hanson, E.; Nwakile, C.; Hammed, V. O. Carbon capture, utilization, and storage (CCUS) technologies: Evaluating the effectiveness of advanced CCUS solutions for reducing CO2 emissions. *Results Surf. Interfaces* **2025**, *18*, 100381.
(41) Hekmatmehr, H.; Esmaeili, A.; Pourmahdi, M.; Saeid Atashrouz, S.; Abedi, A.; Abuswer, M. A.; Nedeljkovic, D.; Latifi, M.; Farag, S.; Mohaddespour, A. Carbon capture technologies: A review on technology readiness level. *Fuel* **2024**, *363*, 130898.
(42) Kuramochi, T.; Ramirez, A.; Turkenburg, W.; Faaij, A. Comparative assessment of CO_2 capture technologies for carbon-intensive industrial processes. *Prog. Energy Combust. Sci.* **2012**, *38* (1), 87−112.
(43) Sifat, N. S.; Haseli, Y. A Critical Review of CO_2 Capture Technologies and Prospects for Clean Power Generation. *Energies* **2019**, *12*, 4143.
(44) Stolaroff, J. K.; Keith, D. W.; Lowry, G. V. Carbon Dioxide Capture from Atmospheric Air Using Sodium Hydroxide Spray. *Environ. Sci. Technol.* **2008**, *42*, 2728−2735.
(45) Mahmoudkhani, M.; Keith, D. W. Low-energy sodium hydroxide recovery for CO2 capture from atmospheric air—Thermodynamic analysis. *Int. J. Greenhouse Gas Control* **2009**, *3*, 376−384.
(46) Ghaffari, S.; Gutierrez, M. F.; Seidel-Morgenstern, A.; Lorenz, H.; Schulze, P. Sodium Hydroxide-Based CO_2 Direct Air Capture for Soda Ash Production—Fundamentals for Process *Engineering. Ind. Eng. Chem. Res.* **2023**, *62*, 7566−7579.
(47) Perez-Lopez, R.; Montes-Hernandez, G.; Nieto, J. M.; Renard, F.; Charlet, L. Carbonation of alkaline paper mill waste to reduce CO2 greenhouse gas emissions into atmosphere. *Appl. Geochem.* **2008**, *23*, 2292−2300.
(48) Crouzet, C.; Brunet, F.; Montes-Hernandez, G.; Recham, N.; Findling, N.; Ferrasse, J. H.; Goffé, B. Hydrothermal Valorization of Steel Slags—Part I: Coupled H2 Production and CO2 mineral Sequestration. *Front. Energy Res.* **2017**, *5*, 29.
(49) Gautier, Q.; Bénézeth, P.; Mavromatis, V.; Schott, J. Hydromagnesite solubility products and growth kinetics in aqueous solution from 25 to 75°C. *Geochem. Cosmochem. Acta* **2014**, *138*, 1−20.
(50) Dreux, G.; Festa, J. *Nouveaux guide du béton et de ces constituants*, 8éme Edition Eyrolles, 1998, ISBN13 978−2-212−10231−4.
(51) Vandamme, M.; Ulm, F. J. Nanogranular origin of concrete creep. *Proc. Natl. Acad. Sci. U. S. A.* **2009**, *106*, 10552−10557.
(52) Chidiac, S. E.; Mahmoodzadeh, F. Plastic viscosity of fresh concrete − A critical review of predictions methods. *Cem. Concr. Compos.* **2009**, *31*, 535−544.
(53) Kovacik, J. Correlation between Young's modulus and porosity in porous materials. *J. Mater. Sci. Lett.* **1999**, *18*, 1007−1010.
(54) Yaman, I. O.; Hearn, N.; Aktan, H. M. Active and non-active porosity in concrete − Part I: Experimental evidence. *Mater. Struct.* **2002**, *35*, 102−109.

https://doi.org/10.1021/acs.iecr.5c00744
Ind. Eng. Chem. Res. XXXX, XXX, XXX−XXX